used to probe the structure and dynamics of biological and chemical systems at the single-molecule level and reveal properties normally obscured in ensemble measurements. With additional improvements in sensitivity, these tools (*8*) can potentially be applicable to NMR-based label-free detection and analysis of single molecules; characterization of structural and conformational changes in systems that are not easily accessible by conventional techniques; and studies of dynamic phenomena, such as protein folding (*29*) and enzyme-substrate interactions at the single-molecule level (*30*).

REFERENCES AND NOTES

1. P. Glover, S. P. Mansfield, *Rep. Prog. Phys.* **65**, 1489–1511 (2002).
2. H. J. Mamin *et al.*, *Science* **339**, 557–560 (2013).
3. T. Staudacher *et al.*, *Science* **339**, 561–563 (2013).
4. A. O. Sushkov *et al.*, *Phys. Rev. Lett.* **113**, 197601 (2014).
5. J. M. Taylor *et al.*, *Nat. Phys.* **4**, 810–816 (2008).
6. L. Childress, R. L. Walsworth, M. D. Lukin, *Phys. Today* **67**, 38–43 (2014).
7. S. Kolkowitz, Q. P. Unterreithmeier, S. D. Bennett, M. D. Lukin, *Phys. Rev. Lett.* **109**, 137601 (2012).
8. Materials, methods, and supplementary text are available as supplementary materials on *Science* Online.
9. L. Jiang *et al.*, *Science* **326**, 267–272 (2009).
10. P. Neumann *et al.*, *Science* **329**, 542–544 (2010).
11. Y. Romach *et al.*, *Phys. Rev. Lett.* **114**, 017601 (2015).
12. Y. Chu *et al.*, *Nano Lett.* **14**, 1982–1986 (2014).
13. M. Kim *et al.*, *Appl. Phys. Lett.* **105**, 042406 (2014).
14. G. Goldstein *et al.*, *Proc. Natl. Acad. Sci. U.S.A.* **72**, 11–15 (1975).
15. S. Vijay-Kumar, C. E. Bugg, W. J. Cook, *J. Mol. Biol.* **194**, 531–544 (1987).
16. J. C. Sheehan, P. A. Cruickshank, G. L. Boshart, *J. Org. Chem.* **26**, 2525–2528 (1961).
17. A. O. Sushkov *et al.*, *Nano Lett.* **14**, 6443–6448 (2014).
18. M. Loretz, S. Pezzagna, J. Meijer, C. L. Degen, *Appl. Phys. Lett.* **104**, 033102 (2014).
19. D. B. Zax, A. Bielecki, K. W. Zilm, A. Pines, D. P. Weitekamp, *J. Chem. Phys.* **83**, 4877–4905 (1985).
20. T. P. Das, E. L. Hahn, *Nuclear Quadrupole Resonance Spectroscopy* (Academic Press, 1958).
21. B. J. Shields, Q. P. Unterreithmeier, N. P. de Leon, H. Park, M. D. Lukin, *Phys. Rev. Lett.* **114**, 136402 (2015).
22. P. London *et al.*, *Phys. Rev. Lett.* **111**, 067601 (2013).
23. T. Staudacher *et al.*, *Nat. Commun.* **6**, 8527 (2015).
24. S. Cavadini, *Prog. Nucl. Magn. Reson. Spectrosc.* **56**, 46–77 (2010).
25. A. Ajoy, U. Bissbort, M. D. Lukin, R. L. Walsworth, P. Cappellaro, *Phys. Rev. X* **5**, 011001 (2015).
26. T. A. Klar, R. Wollhofen, J. Jacak, *Phys. Scr.* **2014**, 014049 (2014).
27. D. Rugar, R. Budakian, H. J. Mamin, B. W. Chui, *Nature* **430**, 329–332 (2004).
28. C. L. Degen, M. Poggio, H. J. Mamin, C. T. Rettner, D. Rugar, *Proc. Natl. Acad. Sci. U.S.A.* **106**, 1313–1317 (2009).
29. H. S. Chung, K. McHale, J. M. Louis, W. A. Eaton, *Science* **335**, 981–984 (2012).
30. I. A. Yudushkin *et al.*, *Science* **315**, 115–119 (2007).

ACKNOWLEDGMENTS

We thank M. L. Pham, N. Chisholm, G. Kucsko, B. Harada, A. Ajoy, and P. Cappellaro for helpful discussions and experimental help. This work was supported by the Defense Advanced Research Projects Agency (QuASAR program), NSF, the Center for Ultracold Atoms, the Army Research Office Multidisciplinary University Research Initiative, the National Security Science and Engineering Faculty Fellowship program, and the Gordon and Betty Moore Foundation. I.L. was supported by the Air Force Office of Scientific Research National Defense Science and Engineering Graduate Fellowship (32 CFR 168a). Work at Ulm University was supported by the European Research Council. L.M. acknowledges support by a German Academic Exchange Service (DAAD) P.R.I.M.E. Fellowship. E.B. was supported by the Herchel Smith–Harvard Undergraduate Summer Research Program.

SUPPLEMENTARY MATERIALS

www.sciencemag.org/content/351/6275/836/suppl/DC1
Materials and Methods
Supplementary Text
Figs. S1 to S10
Table S1
References (*31*–*38*)

3 November 2015; accepted 21 January 2016
Published online 4 February 2016
10.1126/science.aad8022

NANOMATERIALS

DNA-controlled dynamic colloidal nanoparticle systems for mediating cellular interaction

Seiichi Ohta,[1,2] Dylan Glancy,[1,3] Warren C. W. Chan[1,3,4,5]*

Precise control of biosystems requires development of materials that can dynamically change physicochemical properties. Inspired by the ability of proteins to alter their conformation to mediate function, we explored the use of DNA as molecular keys to assemble and transform colloidal nanoparticle systems. The systems consist of a core nanoparticle surrounded by small satellites, the conformation of which can be transformed in response to DNA via a toe-hold displacement mechanism. The conformational changes can alter the optical properties and biological interactions of the assembled nanosystem. Photoluminescent signal is altered by changes in fluorophore-modified particle distance, whereas cellular targeting efficiency is increased 2.5 times by changing the surface display of targeting ligands. These concepts provide strategies for engineering dynamic nanotechnology systems for navigating complex biological environments.

Fundamental studies on the interactions of nanoparticle designs with biomolecules, cells, tissues, and organs are providing guiding principles with which to build nanosystems for imaging, diagnosis, and the treatment of disease. An optimal nanoparticle physicochemical property (for example, size, shape, and surface chemistry) for biological use varies with time and place within the living body, and current nanoparticle designs do not have the engineering range to meet these design requirements (*1*–*3*). For example, rod-shaped particles are reported to be preferable for tumor penetration (*4*), whereas spherical nanoparticles are better for subsequent cellular uptake by cancer cells (*5*); nanoparticles coated with polymer polyethylene glycol (PEG) can increase blood circulation time by reducing serum protein adsorption and macrophage uptake (*6*) but can impede surface-coated antibodies from cell targeting (*7*). These variations have inspired the development of interactive nanoparticle systems that can alter their properties in response to biological stimuli (*8*–*10*). However, dynamic control over the physicochemical properties of nanoparticles, especially particle shape, remains a challenge. DNA provides exquisite control and flexibility in engineering the physicochemical, morphological, optical, and electrical properties of three-dimensional (3D) nanosystems (*11*–*14*). But these DNA-assembled structures have not been fully exploited for cellular and biological application. We explored the use of DNA to assemble shape-shifting nanostructures with controlled biological function.

We used single-stranded DNA–functionalized gold nanoparticles (AuNPs) of different sizes (denoted as large, medium, and small) as building blocks to assemble shape-changing nanostructures (Fig. 1A and fig. S1). Each AuNP was functionalized with two DNA sequences: one for nanostructure assembly and the other for shape-changing (*15*). Valencies of these nanoparticles were 114, 25, and 6 DNA strands on 13-, 6-, and 3-nm AuNPs, respectively (fig. S2). The nanoparticle building blocks were assembled into "core-satellite" structures (*16*, *17*) by a linker DNA strand (L1 and L2) whose ends were complementary to two different nanoparticle types. The assembled nanostructure consists of a large core with surrounding satellites of medium and small size (Fig. 1, assembly morphology 1). An important design feature here is that the linkage between the core and the small satellites contains a single-stranded

[1]Institute of Biomaterials and Biomedical Engineering, Donnelly Center for Cellular and Biomolecular Research, University of Toronto, 164 College Street, Toronto, ON M5S 3G9, Canada. [2]Center for Disease Biology and Integrative Medicine, University of Tokyo, 7-3-1 Hongo, Bunkyo-ku, Tokyo, 113-0033, Japan. [3]Department of Chemistry, University of Toronto, 80 St. George Street, Toronto, ON M5S 3H6, Canada. [4]Department of Chemical Engineering, University of Toronto, 200 College Street, Toronto, ON M5S 3E5, Canada. [5]Department of Material Science and Engineering, University of Toronto, 160 College Street, Room 450, University of Toronto, Toronto, ON M5S 3E1, Canada.
***Corresponding author. E-mail: warren.chan@utoronto.ca**

spacer sequence [17 bases (Fig. 1A, black)], which if precisely designed can allow nanoparticles to change into different shapes via a "toe-hold strand displacement" mechanism (*18*–*20*) to reconfigure the DNA assembly (Fig. 1A). An attaching strand, A1, was first added in order to anchor small satellites to the medium-sized nanoparticles under hybridization and purification conditions. No substantial change in shape was observed with transmission electron microscopy (TEM) at this step (denoted as "intermediate" structure hereafter). Then, $L1_{comp}$, a fully complementary detaching strand to the linker strand between the core and small satellites (L1), was added. Because the duplex formation with $L1_{comp}$ is energetically favorable, L1 was displaced from the superstructure, resulting in the detachment of small satellites from the core. Through these two steps, small satellites were relocated from the core to the medium satellite, transforming the nanoassemblies into a new shape in which medium particles became the new core, surrounded by small satellites (assembly morphology 2). The successful shape change of nanoassemblies mediated by DNA are shown in representative images in Fig. 1B.

The reversibility of the transforming nanoassemblies is shown in Fig. 2A TEM images. The nanoassemblies first changed their assembled shape from morphology 1 to morphology 2 by the addition of A1 and $L1_{comp}$ strands. Similarly, addition of L1 and $A1_{comp}$ allowed the nanoassemblies to revert back to their original shape. The low-magnification TEM images (fig. S3) and ultraviolet-visible absorbance spectra (fig. S4) showed that the nanoassemblies are monodisperse, and dynamic light scattering measurements showed hydrodynamic sizes of 94 and 74 nm for morphologies 1 and 2, respectively (fig. S5). These characterizations indicate that the shape-changing nanoassemblies are colloidally stable in phosphate-buffered saline. We analyzed a larger population of nanoassemblies with TEM to determine the efficiency of the shape shift (Fig. 2A). We defined assembly morphologies 1 and 2 by particle distance, as illustrated in fig. S6. We measured the proximity of 3-nm (small) particles to either 6-nm (medium) or 13-nm (large) particles for each nanoassembly in order to determine its conformation. Structures in which satellites were concentrated near 3-nm particles were categorized as assembly morphology 1, whereas assemblies with 3-nm particles more closely associated with 6-nm cores were classified as morphology 2. Nanoassemblies that met neither of the above criteria were categorized as "other." The analysis showed that conversion of morphology 1 to morphology 2 occurred at an efficiency of 89% and was capable of reverting back to morphology 1 at an efficiency of 88%. During these shape changes, some of the satellites detach from the assembly because of imperfect anchoring; the average number of 6-nm particles on a nanoassembly of morphology 1, morphology 2, and the reversed morphology 1 was 1.8, 1.6, and 1.5, respectively, whereas that of 3-nm particles was 9.7, 6.6, and 5.6, respectively (fig. S7). The shape change was further evaluated by means of 2D radial distribution function (RDF) analysis (*21*). RDF of satellites from a core particle was calculated from the TEM images (Fig. 2B). In morphology 1, a single peak around 16 nm was observed, indicating the isotropic position of 3- and 6-nm satellites with respect to the 13-nm core. On the other hand, broadened multiple peaks were observed in morphology 2, which reflected the new position of 3-nm satellites. This RDF reverted back to the single peak after adding L1 and $A1_{comp}$ strands. These differences confirmed the reversible shape change of nanoassemblies. The shape change was not induced by the addition of DNA that has a noncomplementary sequence (fig. S8), suggesting specificity of this system. This shape-shifting property was not limited to a single design. By changing the linker stoichiometry, we successfully generated core-satellite structures with various numbers of 6-nm secondary cores (two to four) (fig. S9). Using the same procedures, each of the base structures could successfully change their shape (Fig. 2C).

We next determined whether the optical properties of the nanoassemblies could be controlled through morphological changes. The optical properties of a nanoparticle, such as fluorescence and surface plasmon resonance, are sensitive to the location of neighboring particles. For example, changes in the distance of neighboring fluorescent nanoparticles can alter their Förster resonance energy transfer (FRET) signals (*22*, *23*). The overall principle of our experiment is described in Fig. 3A. DNA strands on 13-, 6-, and 3-nm building block particles were end-labeled with fluorescein amidite (FAM), Cy5, or Cy3, respectively, then coated onto the nanoparticle

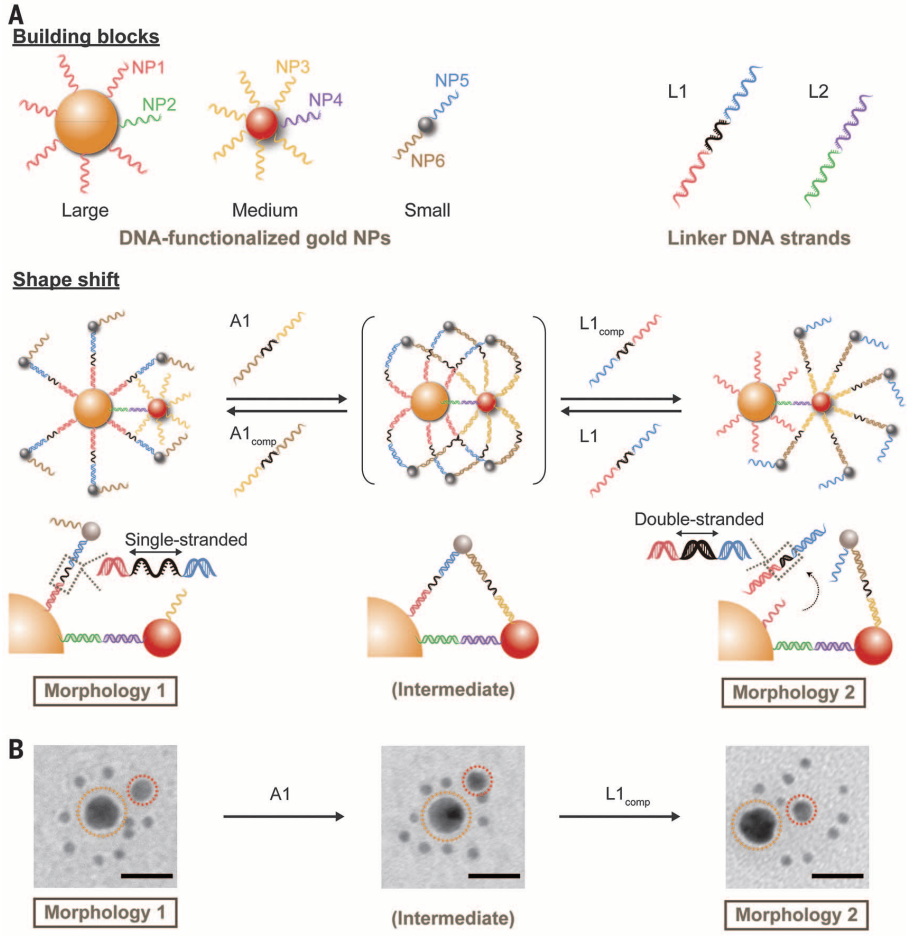

Fig. 1. Schematic illustration and corresponding TEM images of the shape change of nanoparticle assemblies mediated by DNA. (**A**) Individual nanoparticles (large, medium, and small) were functionalized with strands of two distinct single-stranded DNA sequences (NP1 to NP6). By using linker DNA strands containing complementary sequence regions (L1 and L2), they were then assembled into the core-satellite structure (assembly morphology 1). To change the shape of the nanoassembly, attaching strands (A1) were added to anchor small satellites to the medium particle (intermediate). After that, the detaching strand ($L1_{comp}$) was added to dislocate L1, resulting in the relocation of small satellites from the large core to the medium satellites (assembly morphology 2). This shape change can be reversed by adding extra attaching and detaching strands, L1 and $A1_{comp}$. For clarity, the schematics represent a cross-section of the 3D nanoassemblies that are composed of core particles surrounded by satellite particles. (**B**) Representative TEM images of the nanoassemblies of morphology 1, intermediate, and morphology 2. They consist of 13-, 6-, and 3-nm gold nanoparticles. The orange and red circles indicate a 13- and 6-nm particle, respectively. Scale bar, 20 nm.

and assembled. Given that the 3-nm particles are anchored to the 13-nm core in morphology 1, FAM and Cy3 are close enough to induce FRET. When we excite FAM, florescence from Cy3 can be observed. However, no FRET is observed by the excitation of Cy3 because the 3- and 6-nm particles are farther from one another. After shifting to the intermediate structure, FRET can be observed with the excitation of either FAM or Cy3 as 3-nm particles are anchored to both 13- and 6-nm particles. When the shape is finally shifted to morphology 2, FRET can be detected only through Cy3 excitation because 3-nm particles are now detached from the 13-nm core. Experimentally, DNA strands were fluorescently labeled according to supplier, coated onto the AuNPs, and purified, and the photoluminescent spectra were measured in order to verify successful coating (fig. S10). Because strands NP1 to NP6 were composed of 25 bases, which roughly corresponds to 5 to 10 kDa of linear polymer chain, they are remote enough to prevent fluorescent quenching by AuNPs (*24*). Photoluminescent spectra of the assembled nanostructures are shown in Fig. 3, B and C, at each step of the shape-changing process. After excitation of FAM, a prominent signal from Cy3 was observed at 561 nm for assembly morphology 1 and the intermediate structure (Fig. 3B). This signal was decreased after shifting to morphology 2. After Cy3 excitation, the shift from morphology 1 to the intermediate shape was accompanied by the emergence of the signal from Cy5 at 665 nm, but the subsequent shift to morphology 2 did not affect the signal (Fig. 3C). These changes in FRET signals are consistent with the expected position of fluorophores (Fig. 3A), validating our proposed mechanism. Real-time monitoring of the shape shift was also carried out with FRET measurement (Fig. 3D). A1 and $L1_{comp}$ strands were sequentially added to the nanoassemblies in a hybridization buffer, during which the changes in fluorescent signals from Cy3 and Cy5—obtained through the excitation of FAM and Cy3, respectively—were measured in real time at room temperature. The signals from Cy3 and Cy5 respond specifically to the addition of the attaching and detaching strands, illustrating the fidelity of the shape change. We found that each step of the transformation is predominantly complete within 10 min. Assuming first-order reaction kinetics, the reaction rate constant for the first and the second step of the shape change was estimated to be 1.9×10^{-3} and 1.7×10^{-3} s^{-1}, respectively (fig. S11). These results not only confirm successful shape-shifting of the nanoassemblies but also suggest possible applications as imaging probes that are responsive to specific DNA sequences.

Last, we determined whether we could alter the cellular interaction of our nanoassemblies by changing their shape and thus, indirectly, changing the presentation of the surface chemistry. This is an important feature because the optimal physicochemical properties to mediate transport in cells, tissues, and whole animals necessitate particles of different sizes, shapes, and surface chemistries (*4*–*7*). It is unlikely that current single-particle design systems will be able to fulfill these engineering requirements. We controlled the presentation of targeting ligands on the surface of the nanoassembly system by changing its shape via DNA. We functionalized the core particle with folic acid

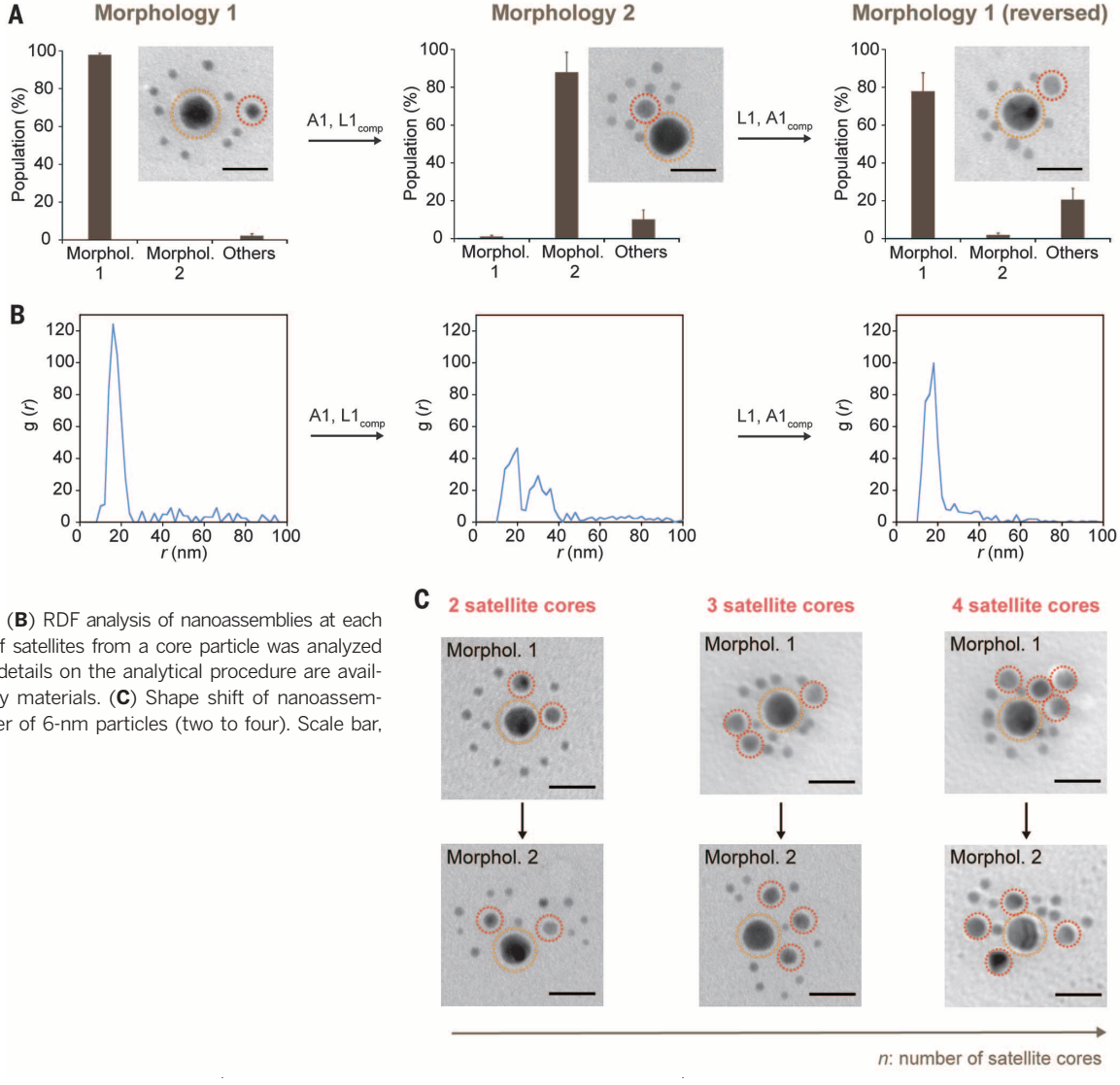

Fig. 2. Reversibility and design versatility of the nanoassembly shape change. (**A**) TEM images and histograms of the nanoparticle assemblies at each shape-shifting step. Scale bar, 20 nm. The shape of the nanoassembly was categorized as assembly morphology 1, 2, and others by particle distance (the definition is provided in fig. S6), and then the proportion of each shape was analyzed from TEM images. More than 100 assemblies were analyzed for each condition. (**B**) RDF analysis of nanoassemblies at each shape-shifting step. RDF of satellites from a core particle was analyzed from TEM images. More details on the analytical procedure are available in the supplementary materials. (**C**) Shape shift of nanoassemblies with different number of 6-nm particles (two to four). Scale bar, 20 nm.

(FA) as a targeting ligand for overexpressed folate receptor in many types of cancer cells (Fig. 4A) (*25*). In assembly morphology 1, FAs are surrounded by 3- and 6-nm satellites, which sterically hinder their targeting ability (OFF state). After transformation to morphology 2, "hidden" FAs are exposed to the outer environment via the relocation of 3-nm satellites, activating the targeting property of the nanoassemblies (ON state).

The FA functionalization was achieved by concurrently conjugating FA-functionalized PEG [molecular weight (M_w) = 5 kDa] terminated with thiol and DNA strands to 13-nm particles. The resulting grafting density was 40.0 ± 5.2 FA molecules per particle. The cellular uptake of the FA-functionalized nanoassemblies was examined by using folate receptor–expressing U87-MG human glioblastoma-astrocytoma cells (*25*, *26*). The cells were incubated with the nanoassemblies of morphology 1 or 2 in serum-free media, as described in the supplementary materials, materials and methods. Serum was not added to the media so as to avoid the interaction of nonspecifically adsorbed serum proteins with nanoparticles and influencing cellular interaction (*27*). TEM images of the nanoassemblies internalized by U87-MG cells are shown in Fig. 4, B and C. Nanoparticles were found within vesicles inside the cells, suggesting that they were internalized via endocytosis. Moreover, as we reported (*28*), the nanostructures were disassembled into their respective building blocks in the vesicles, whereas fully assembled nanostructures were still found in the culture media.

We quantified the amount of cellular uptake by means of inductively coupled plasma mass spectrometry (ICP-MS). Nanoassemblies conjugated with the same amount of PEG but without FA functionalization were used as a control. ICP-MS revealed that the cellular uptake of FA-conjugated nanoassemblies of morphology 2 was 2.5 times higher than that of morphology 1, indicating the ON/OFF switching of the targeting property. It was also found that the ON/OFF switching was moderately effective even without FA functionalization; the cellular uptake of morphology 2 was 1.5 times higher than that of morphology 1 (Fig. 4D). We deduced that both shape and surface chemistry (type of DNA sequences exposed on the outer surface) of the nontargeted nanoassembly is responsible for this difference (figs. S14 and S15). This effect is amplified by the FA conjugation. A competition experiment was conducted in order to confirm the contribution of FA functionalization in cellular uptake. Free FA was added to the culture media with the nanoassemblies (Fig. 4E). The ON/OFF ratio of the control nanoassemblies exhibited little change in the presence of free FA. Conversely, for FA-functionalized assemblies, the ON/OFF ratio substantially decreased with increasing free FA concentration toward control level, suggesting that the cellular uptake was indeed mediated by FA-folate receptor interaction. These results demonstrate that DNA-mediated shape change of the nanoassembly can alter the surface display of targeting ligands and thus control its cellular uptake property.

Some natural biomolecules, such as proteins, switch their function by changing their 3D conformation in response to biological signals. This quality allows them to display varying conformations to activate functions or stay dormant until needed. Like these biomolecules, the nanoassemblies presented here alter their fluorescent and cellular uptake properties by transforming their structure in response to specific DNA sequences. A next step is to design the linker sequences to respond to circulating DNA or intracellular RNA sequences and to determine the impact of payload on shape-shifting property. Although further development is needed for their practical use, the concept presented here can be expanded to develop more complex systems that can mimic the diverse functions of a protein to selectively control the biological functions of the engineered nanosystem. Our proposed design strategy provides a new opportunity and general method with which to develop future dynamic nanomaterials that can travel through the blood stream and into diseased sites, transforming into the required shapes to overcome diverse biological barriers and activating their function to diagnose or treat targeted sites.

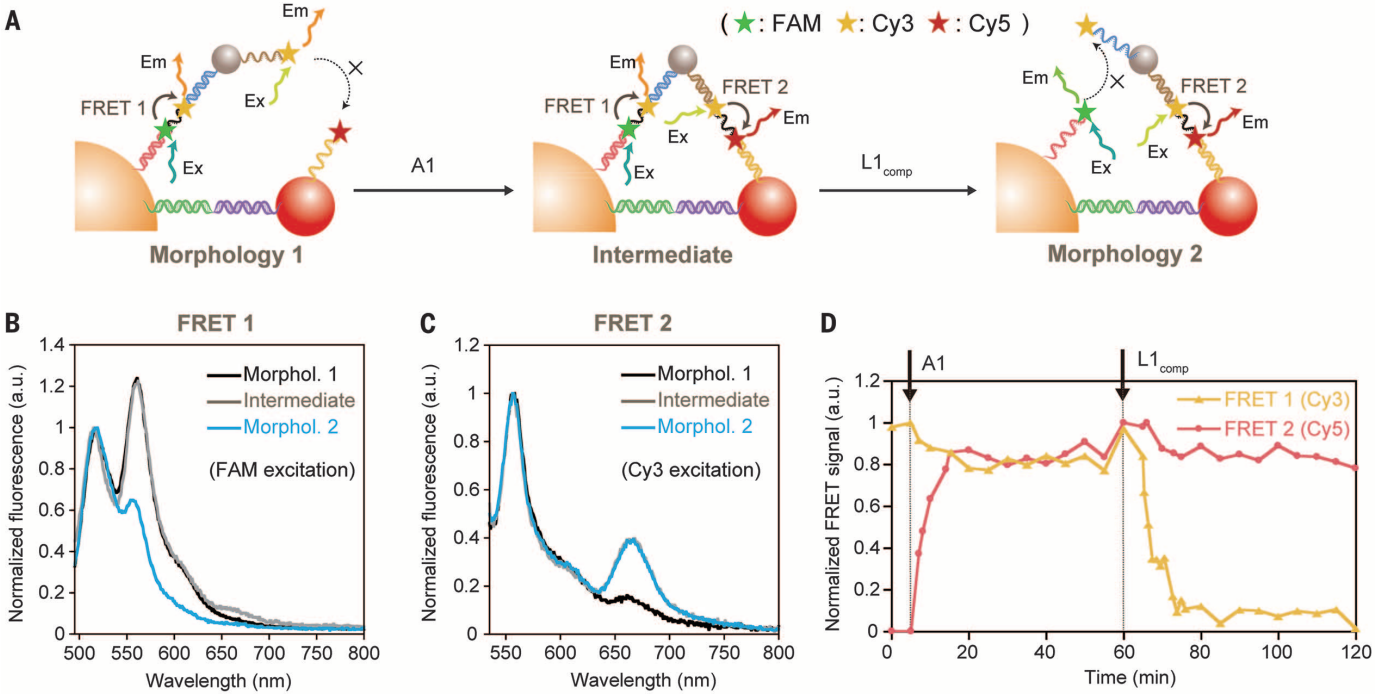

Fig. 3. Changes in FRET signals from the nanoparticle assemblies induced by shape change. (**A**) Schematic illustration of the FRET occurring in the nanoassemblies. In assembly morphology 1, FRET between FAM and Cy3 (FRET 1) can be observed through excitation of FAM, whereas FRET between Cy3 and Cy5 (FRET 2) does not occur through excitation of Cy3. After the shift to intermediate structure, FRET is observed between FAM and Cy3 and between Cy3 and Cy5. Then, in morphology 2, FRET can be detected only between Cy3 and Cy5. (**B** and **C**) Photoluminescent spectra from nanoassemblies (morphology 1, intermediate, and morphology 2). They are excited at (B) 480 nm for FAM or (C) 520 nm for Cy3. Each spectrum is normalized to the peak from (B) FAM at 519 nm or that from (C) Cy3 at 561 nm, respectively. (**D**) Real-time monitoring of FRET signals during the shape change. A1 and $L1_{comp}$ DNA strands were added at 5 and 60 min, respectively, to the nanostructure solution, whereas FRET signals from Cy3 (FRET 1, excitation at 480 nm) and Cy5 (FRET 2, excitation at 520 nm) were monitored in real time.

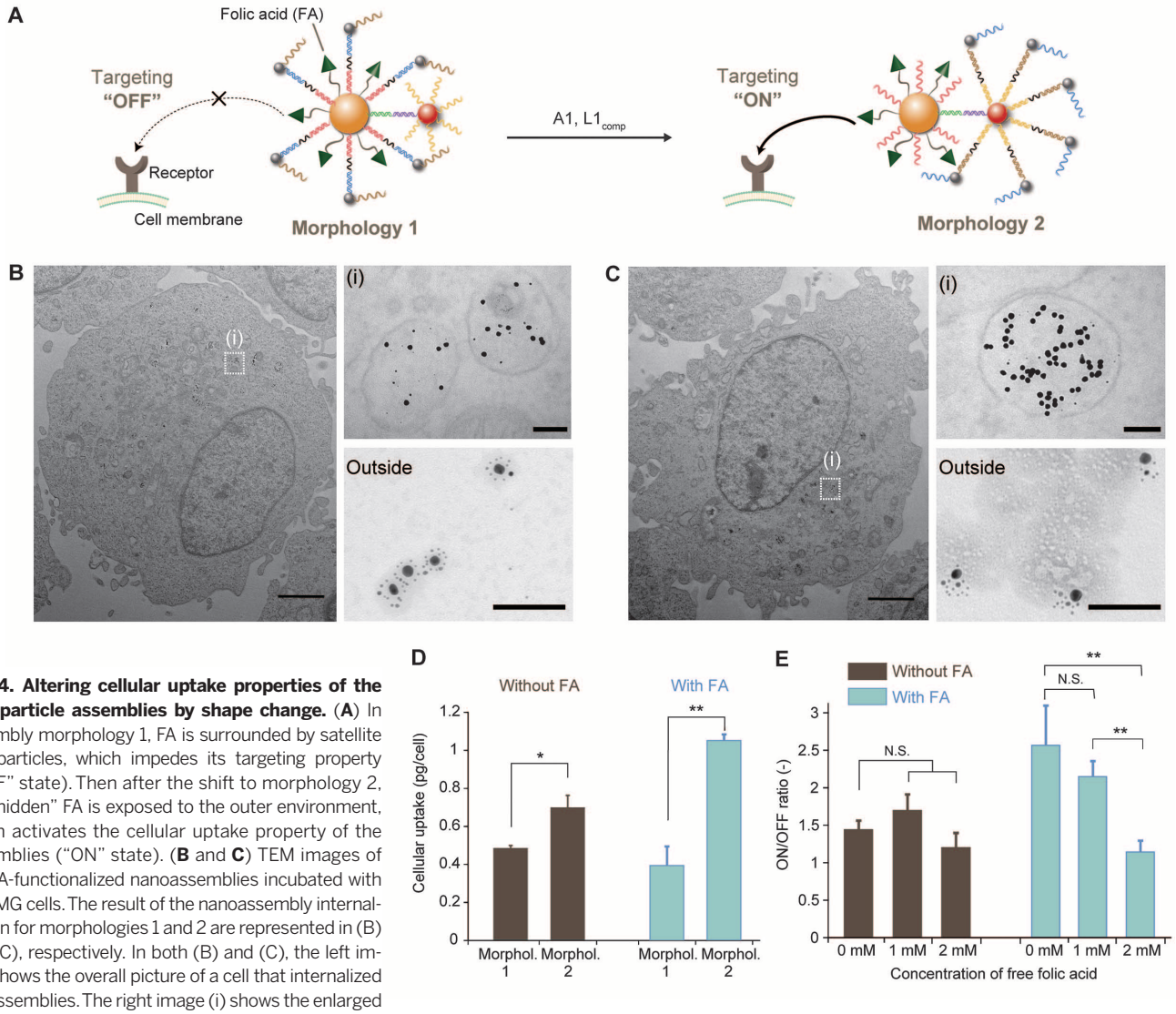

Fig. 4. Altering cellular uptake properties of the nanoparticle assemblies by shape change. (**A**) In assembly morphology 1, FA is surrounded by satellite nanoparticles, which impedes its targeting property ("OFF" state). Then after the shift to morphology 2, the "hidden" FA is exposed to the outer environment, which activates the cellular uptake property of the assemblies ("ON" state). (**B** and **C**) TEM images of the FA-functionalized nanoassemblies incubated with U87-MG cells. The result of the nanoassembly internalization for morphologies 1 and 2 are represented in (B) and (C), respectively. In both (B) and (C), the left image shows the overall picture of a cell that internalized the assemblies. The right image (i) shows the enlarged image of its corresponding part of the overall picture. The nanoassemblies found in the culture media after the incubation are also shown. Scale bars, 2.0 μm (low-magnification images) and 100 nm (enlarged images). More enlarged images inside cells are provided in fig. S12. Nanoassemblies without FA functionalization are provided in fig. S13. (**D**) Comparison of the amount of cellular uptake of the FA-functionalized nanoassemblies between morphology 1 and morphology 2 measured with ICP-MS. Nanoassemblies without FA functionalization were also used as controls. Data are averages ± SD ($n > 3$ experimental replicates). (**E**) Effect of free FA on the ON/OFF switching ratio of the cellular uptake. The ON/OFF ratio was defined as the ratio of the amount of cellular uptake of the assemblies between morphology 2 and morphology 1 (raw data are shown in fig. S16). Data are averages ± SD ($n > 3$ experimental replicates). $^{**}P < 0.01$, $^{*}P < 0.05$. N.S., not significant.

REFERENCES AND NOTES

1. W. Jiang, B. Y. Kim, J. T. Rutka, W. C. Chan, *Nat. Nanotechnol.* **3**, 145–150 (2008).
2. R. A. Petros, J. M. DeSimone, *Nat. Rev. Drug Discov.* **9**, 615–627 (2010).
3. H. Cabral *et al.*, *Nat. Nanotechnol.* **6**, 815–823 (2011).
4. V. P. Chauhan *et al.*, *Angew. Chem. Int. Ed. Engl.* **50**, 11417–11420 (2011).
5. B. D. Chithrani, A. A. Ghazani, W. C. Chan, *Nano Lett.* **6**, 662–668 (2006).
6. K. Knop, R. Hoogenboom, D. Fischer, U. S. Schubert, *Angew. Chem. Int. Ed. Engl.* **49**, 6288–6308 (2010).
7. Q. Dai, C. Walkey, W. C. Chan, *Angew. Chem. Int. Ed. Engl.* **53**, 5093–5096 (2014).
8. C. Wong *et al.*, *Proc. Natl. Acad. Sci. U.S.A.* **108**, 2426–2431 (2011).
9. G. von Maltzahn *et al.*, *Nat. Mater.* **10**, 545–552 (2011).
10. J. W. Yoo, S. Mitragotri, *Proc. Natl. Acad. Sci. U.S.A.* **107**, 11205–11210 (2010).
11. M. R. Jones, N. C. Seeman, C. A. Mirkin, *Science* **347**, 1260901 (2015).
12. A. Kuzyk *et al.*, *Nature* **483**, 311–314 (2012).
13. Y. Zhang *et al.*, *Nat. Mater.* **14**, 840–847 (2015).
14. S. M. Douglas, I. Bachelet, G. M. Church, *Science* **335**, 831–834 (2012).
15. X. Zhang, M. R. Servos, J. Liu, *J. Am. Chem. Soc.* **134**, 7266–7269 (2012).
16. X. Xu, N. L. Rosi, Y. Wang, F. Huo, C. A. Mirkin, *J. Am. Chem. Soc.* **128**, 9286–9287 (2006).
17. J. H. Yoon, J. Lim, S. Yoon, *ACS Nano* **6**, 7199–7208 (2012).
18. D. Y. Zhang, G. Seelig, *Nat. Chem.* **3**, 103–113 (2011).
19. B. Yurke, A. J. Turberfield, A. P. Mills Jr., F. C. Simmel, J. L. Neumann, *Nature* **406**, 605–608 (2000).
20. Y. Tian, C. Mao, *J. Am. Chem. Soc.* **126**, 11410–11411 (2004).
21. X. Yu *et al.*, *Nano Today* **8**, 480–493 (2013).
22. C. S. Yun *et al.*, *J. Am. Chem. Soc.* **127**, 3115–3119 (2005).
23. P. D. Howes, R. Chandrawati, M. M. Stevens, *Science* **346**, 1247390 (2014).
24. L. Y. Chou, W. C. Chan, *Adv. Healthc. Mater.* **1**, 714–721 (2012).
25. Z. Xu *et al.*, *Int. J. Pharm.* **426**, 182–192 (2012).
26. J. Zhu *et al.*, *Biomaterials* **35**, 7635–7646 (2014).
27. C. D. Walkey *et al.*, *ACS Nano* **8**, 2439–2455 (2014).
28. L. Y. Chou, K. Zagorovsky, W. C. Chan, *Nat. Nanotechnol.* **9**, 148–155 (2014).

ACKNOWLEDGMENTS

W.C.W.C. acknowledges the Natural Sciences and Engineering Research Council (NSERC) for support (2014-06397), Canadian Institute of Health Research (MOP-130143), and Prostate Cancer Canada (D2014-12). S.O. acknowledges the Japan Society for the Promotion of Science (JSPS) for a Research Fellowship (PD, no. 5621) and the Ministry of Education, Culture, Sports, Science and Technology (MEXT) of Japan for a Grant-in-Aid for Young Scientists (B, no. 26820356). D.G. acknowledges NSERC for a graduate fellowship. The authors thank the Advanced Bioimaging Centre at Mount Sinai Hospital for the use of the TEM and Toronto Nanofabrication Center at University of Toronto for the use of ICP-MS. The authors also thank L. Chou for interesting discussions.

SUPPLEMENTARY MATERIALS

www.sciencemag.org/content/351/6275/841/suppl/DC1
Materials and Methods
Figs. S1 to S16
References (*29*–*31*)

19 September 2015; accepted 15 January 2016
10.1126/science.aad4925

Science

DNA-controlled dynamic colloidal nanoparticle systems for mediating cellular interaction

Seiichi Ohta, Dylan Glancy and Warren C. W. Chan

Science **351** (6275), 841-845.
DOI: 10.1126/science.aad4925

Dynamic DNA clustering of nanoparticles

The size and shape of nanoparticles can increase the cellular uptake and delivery of contrast agents and therapeutics. Ohta *et al.* created gold nanoparticles partly covered with DNA chains and with folic acid as the targeting molecule (see the Perspective by Parak). The particles could link together to hide the folic acid or to expose it on the surface, depending on the hybridization and overall particle configuration. The addition of complementary DNA allowed switching between structures, thus changing the way the particles interacted with cells.

Science, this issue p. 841; see also p. 814

Science (print ISSN 0036-8075; online ISSN 1095-9203) is published by the American Association for the Advancement of Science, 1200 New York Avenue NW, Washington, DC 20005. The title *Science* is a registered trademark of AAAS.